Inorganic Chemistry

Article

pubs.acs.org/IC

Sensitivity of X-ray Core Spectroscopy to Changes in Metal Ligation: A Systematic Study of Low-Coordinate, High-Spin Ferrous Complexes

P. Chandrasekaran,[†,▽] Karen P. Chiang,[‡] Dennis Nordlund,[§] Uwe Bergmann,[∥] Patrick L. Holland,*[,‡] and Serena DeBeer*[,†,⊥]

[†]Department of Chemistry and Chemical Biology, Cornell University, Ithaca, New York 14853, United States

[‡]Department of Chemistry, University of Rochester, Rochester, New York 14627, United States

[§]Stanford Synchrotron Radiation Lightsource, SLAC National Accelerator Laboratory, Menlo Park, California 94025, United States

[∥]Linac Coherent Light Source, SLAC National Accelerator Laboratory, Menlo Park, California 94025, United States

[⊥]Max Planck Institute for Chemical Energy Conversion, Stiftstrasse 34-36, D-45470 Mülheim an der Ruhr, Germany

[▽]Department of Chemistry and Biochemistry, Lamar University, Beaumont, Texas 77710, United States

Supporting Information

ABSTRACT: In order to assess the sensitivity and complementarity of X-ray absorption and emission spectroscopies for determining changes in the metal ligation sphere, a systematic experimental and theoretical study of iron model complexes has been carried out. A series of high-spin ferrous complexes, in which the ligation sphere has been varied from a three-coordinate complex, [L^{tBu}Fe(SPh)] (**1**) (where L^{tBu} = bulky β-diketiminate ligand; SPh = phenyl thiolate) to four-coordinate complexes [L^{tBu}Fe(SPh)(X)] (where X = CN^{t}Bu (**2**); 1-methylimidazole (**3**); or *N*,*N*-dimethylformamide (DMF) (**4**)), has been investigated using a combination of Fe K-edge X-ray absorption (XAS) and Kβ X-ray emission (XES) spectroscopies. The Fe K XAS pre-edge and edge of all four complexes are consistent with a high-spin ferrous assignment, with the largest differences in the pre-edge intensities attributed to changes in covalency of the fourth coordination site. The X-ray emission spectra show pronounced changes in the valence to core region (V2C) as the identity of the coordinated ligand is varied. The experimental results have been correlated to density functional theory (DFT) calculations, to understand key molecular orbital contributions to the observed absorption and emission features. The calculations also have been extended to a series of hypothetical high-spin iron complexes to understand the sensitivity of XAS and XES techniques to different ligand protonation states ([L^{tBu}Fe^{II}(SPh)(NH$_n$)]$^{3-n}$ (n = 3, 2, 1, 0)), metal oxidation states [L^{tBu}Fe(SPh)(N)]$^{n-}$ (n = 3, 2, 1), and changes in the ligand identity [L^{tBu}Fe^{IV}(SPh)(X)]$^{n-}$ (X = C^{4-}, N^{3-}, O^{2-}; n = 2, 1, 0). This study demonstrates that XAS pre-edge data have greater sensitivity to changes in oxidation state, while valence to core (V2C) XES data provide a more sensitive probe of ligand identity and protonation state. The combination of multiple X-ray spectroscopic methods with DFT results thus has the potential to provide for detailed characterization of complex inorganic systems in both chemical and biological catalysis.

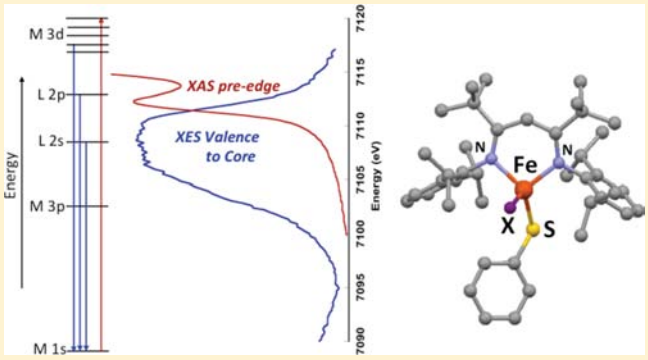

INTRODUCTION

The ability to characterize the changes that occur at transition-metal active sites within catalytic systems is essential for obtaining fundamental insights into the mechanisms of catalysis.[1,2] Spectroscopy has played a key role in the experimental determination of metal oxidation states, spin states, and metal−ligand distances.[3,4] Synchrotron spectroscopy has had a particularly large impact, due to both its element selectivity and the ability to obtain data on samples in almost any physical form.[5,6] Metal K-edge X-ray absorption spectroscopy (XAS) provides a measure of the oxidation state, spin state, and local geometric environment of a transition-metal absorber.[7,8] Beyond the rising edge, the extended X-ray absorption fine structure (EXAFS) region provides metal−ligand bond lengths (within ∼0.01 Å) and scatterer identities (±1 in Z for the first row elements).[9,10] By combining EXAFS and XANES analyses, a more detailed picture of the structure surrounding a transition-metal absorber emerges. However, there are inherent limitations in these methods. The resolution of EXAFS is such that similar scatters within ∼0.1−0.15 Å of each other typically cannot be separated.[11,12] Similarly, no

Received: October 5, 2012
Published: May 10, 2013

   dx.doi.org/10.1021/ic3021723 | *Inorg. Chem.* 2013, 52, 6286−6298

direct information about protonation states is available, so it is often inferred indirectly from EXAFS distances and/or pre-edge intensities.[13,14] Metal Kβ valence to core X-ray emission spectroscopy (XES) is an emerging technique, which shows promise for more direct access to ligand identities and protonation states.[15,16]

X-ray emission phenomena have been known for some time. The earliest reports of Kβ emission lines were in the 1920s,[17] with subsequent applications in the 1950s focused primarily on metal oxides.[18] These initial applications focused on the "Kβ main lines", which arise from the emission upon a metal 3p electron refilling a metal 1s core hole. Due to the strong 3p−3d exchange interaction, the Kβ main lines have a pronounced sensitivity to the metal spin state. To higher energy is the so-called valence to core X-ray emission region (V2C XES) of the spectrum.[19] This region results from ligand valence electrons refilling the metal 1s core hole. As such, these transitions are formally forbidden, but they gain intensity through a small amount of metal *n*p character mixed into the ligand orbitals.[20] The V2C XES transitions are thus inherently weak, but they provide direct access to ligand based molecular orbitals, in a manner analogous to photoelectron spectroscopy, but without the requirements for high-vacuum conditions.[21] In recent years, more intense synchrotron sources and beamlines dedicated to XES measurements have improved the experimental conditions for V2C XES, allowing this promising technique to be applied to dilute catalytic systems. In 2010, the first report of V2C XES applied to a biological catalyst was reported by Pushkar et al.[22] In this study, V2C XES was applied to the tetranuclear Mn site in photosystem II and provided experimental evidence for the presence of Mn−oxo bridges, based on the presence of a Kβ'' (ligand 2s to metal 1s) satellite feature. In Pushkar's study, the analysis was largely empirical and no interpretation of the ligand 2p to 1s region was given. Recently, we and others have shown that simple density functional theory (DFT) methods can be used to model the entire V2C XES region.[15,23,24] This approach was also applied by Lancaster et al.[25] to the FeMoco site of nitrogenase and used to provide evidence for a central carbide ligand—a finding that had not previously been accessible by other spectroscopic methods. The work of Pushkar and Lancaster provides clear examples of the power of the V2C XES method. However, many questions remain about the sensitivity of V2C XES and its complementarity to more widely used X-ray methods, such as metal K-edge XAS.

In the present study, we explore these questions through systematic XAS and XES studies on a series of high-spin Fe(II) complexes, where the ligand environment is systematically varied. Namely, we investigate complexes of the type [L^{tBu}Fe(SPh)X] (where L^{tBu} = bulky β-diketiminate ligand, SPh = phenylthiolate, and X = none (**1**); X = CN^tBu, *tert*-butyl isocyanide (**2**); X = MeIm, *N*-methylimidazole (**3**); or X = DMF, *N*,*N*-dimethylformamide (**4**)), as shown in Figure 1.[26] These high-spin iron(II) complexes share a trigonal pyramidal coordination sphere that has two nitrogen atoms from a supporting β-diketiminate ligand, as well as a thiolate sulfur atom, in the basal plane. In the apical position of the pyramid are neutral donors that coordinate through different atoms, providing a series where one coordination site is varied from C- to N- to O-based ligation. These well-characterized iron complexes serve as a reference system for understanding the sensitivity of both XES and XAS techniques to systematic changes in the metal coordination site, while maintaining the same oxidation state and an otherwise similar ligand environment. The variations in the XAS pre-edge, as well as the changes in the Kβ main line and the V2C XES, are investigated. The experimental results are correlated to calculated spectra, using DFT and time-dependent DFT (TDDFT) approaches. Given the agreement between theory and experiment, we then extend our experimental studies to a series of hypothetical multiply bonded complexes with relevance to transition-metal-mediated catalysis. The relative strengths and weaknesses of each spectroscopic method for evaluating changes at both the metal and the ligand are assessed. The overall complementarity of multiple spectroscopic approaches correlated to theory is highlighted. The potential of such an integrated approach for future studies in biological and chemical catalysis is discussed.

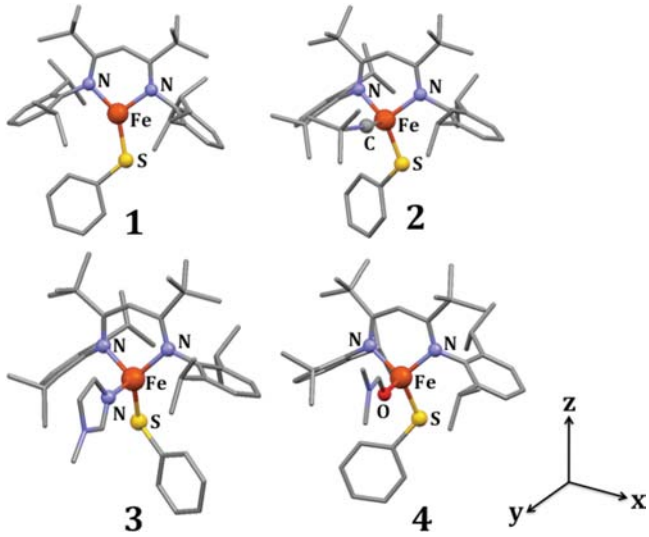

Figure 1. Structures of Fe(II) complexes used in the present study. The [N_2S] ligand frame for all the complexes lies within the *xz* plane, whereas the fourth coordinated ligand lies near the *y* axis.

EXPERIMENTAL SECTION

Sample Preparation. Complexes [L^{tBu}Fe(SPh)] (**1**), [L^{tBu}Fe(SPh)(CN^tBu)] (**2**), [L^{tBu}Fe(SPh)(MeIm)] (**3**), and [L^{tBu}Fe(SPh)(DMF)] (**4**) (where L^{tBu} = bulky β-diketiminate ligand, CN^tBu = *tert*-butyl isocyanide, MeIm = *N*-methylimidazole, DMF = *N*,*N*-dimethylformamide) were synthesized according to published procedures.[26] Samples for XAS and XES studies were prepared by dilution in graphite, pressed into a pellet, and sealed between 38 μm Kapton tape windows in a 1 mm aluminum spacer. All samples were prepared and handled under a dry N_2 atmosphere.

X-ray Absorption Spectroscopy. XAS data were recorded at the Stanford Synchrotron Radiation Lightsource (SSRL) on focused beamline 9−3, under ring conditions of 3 GeV and 60−100 mA. A Si(220) double-crystal monochromator was used for energy selection, and a Rh-coated mirror (set to an energy cutoff of 10 keV) was used for harmonic rejection. Internal energy calibration was performed by assigning the first inflection point of a Fe foil spectrum to 7111.2 eV. XAS data were measured in transmission mode to k = 14 Å^{-1}. The data represent 2−5 scan averages. Data were averaged using EXAFSPAK and splined using PySpline, as described previously.[27] Samples were positioned at 45° with respect to the incident beam and were maintained at a temperature of 20 K in an Oxford CF1208 continuous-flow liquid helium cryostat. No evidence for photoreduction was observed during the course of data collection.

X-ray Emission Spectroscopy. XES data were collected at SSRL beamline 6-2. The incident X-ray energy was tuned to 9 keV utilizing a Si(111) liquid nitrogen cooled monochromator. Vertical and horizontal focusing mirrors were utilized to achieve a beam size of 200 μm × 800 μm with a flux of ~4 × 10^{12} photons/s at 100 mA. The

dx.doi.org/10.1021/ic3021723 | *Inorg. Chem.* 2013, 52, 6286−6298

Table 1. List of Iron Complexes Used in the Present Study and Important Structural and Electronic Details[a]

compd	Fe coord sphere	Fe oxid state	Fe spin state	Fe−X (Å)	Fe−S (Å)	Fe−N (Å)	τ_4[b,37]
1	N, N, S	II	2		2.241 (2.253)	1.945 (1.964)	
2	N, N, S, C	II	2	1.993 (2.089)	2.280 (2.277)	2.011 (2.065)	0.84 (0.80)
3	N, N, S, N	II	2	2.095 (2.094)	2.278 (2.296)	2.006 (2.024)	0.86 (0.85)
4	N, N, S, O	II	2	2.096 (2.083)	2.270 (2.288)	1.995 (2.083)	0.84 (0.81)
$[L^{tBu}Fe(SPh)(NH_3)]$	N, N, S, NH_3	II	2	2.152	2.276	1.996	0.84
$[L^{tBu}Fe(SPh)(NH_2)]^-$	N, N, S, NH_2	II	2	1.954	2.357	2.034	0.89
$[L^{tBu}Fe(SPh)(NH)]^{2-}$	N, N, S, NH	II	2	1.840	2.501	2.000	0.88
$[L^{tBu}Fe(SPh)(N)]^{3-}$	N, N, S, N	II	2	1.679	2.611	2.038	0.75
$[L^{tBu}Fe(SPh)(N)]^{2-}$	N, N, S, N	III	5/2	1.739	2.395	2.120	0.93
$[L^{tBu}Fe(SPh)(C)]^{2-}$	N, N, S, C	IV	2	1.647	2.410	2.015	0.89
$[L^{tBu}Fe(SPh)(N)]^-$	N, N, S, N	IV	2	1.668	2.235	2.047	0.96
$[L^{tBu}Fe(SPh)(O)]$	N, N, S, O	IV	2	1.655	2.221	1.978	0.74

[a]Crystallographic structural parameters are presented in parentheses. [b]Four coordinate geometry index $\tau_4 = 360° - (\alpha + \beta)/141°$; α and β are the largest angles at iron.

energy of the incident beam was calibrated with an iron foil, setting the first inflection point to 7111.2 eV.

XES spectra were recorded with a crystal array spectrometer, which utilizes spherically bent Ge(620) crystals (100 mm diameter, 1 m radius of curvature) aligned on intersecting Rowland circles. An energy resolving Si drift detector (Vortex or Ketek) with a 3 mm vertical slit was used as the X-ray photon detector. Samples were positioned at 45° with respect to the incident beam and were maintained at a temperature of 10 K in an Oxford CF1208 continuous-flow liquid helium cryostat. A helium-filled flight path was utilized between the cryostat and the spectrometer to minimize signal attenuation of the fluorescence.

Iron Kβ XES spectra were collected from 7020 to 7120 eV, with a step size of ∼0.2 eV over the K$\beta_{1,3}$ main line (7020−7070 eV) and steps of ∼0.15 eV over the valence to core region (7070−7120 eV). Spectra were normalized to the incident flux I_0 measured in a He filled ion chamber. The spectrometer energy was calibrated by measuring the energy of the elastically scattered beam as a function of spectrometer position. Fe_2O_3 was used as a reference sample for calibrating the spectrometer energy between different experimental runs, with the maximum of the K$\beta_{1,3}$ main line set to 7060.6 eV and the maximum of the K$\beta_{2,5}$ line set to 7107.2 eV.

For all samples, radiation damage studies were performed to determine the maximum exposure time per spot. Multiple spots were utilized on each sample, and the averaged data represent only those scans which showed no evidence of radiation damage. A maximum dwell time of 30 min per spot was determined as the upper limit for exposure. The total integrated area of the averaged spectra was normalized to a value of 1000.

Data Analysis. The EDG_FIT program was used to quantify pre-edge areas using linear least-squares fits.[28] The pre-edge features were modeled with line shapes having fixed mixing ratio (50:50) of Lorentzian and Gaussian functions (pseudo-Voigt). The background was modeled with both a fixed pseudo-Voigt function (50:50) and a function where the mixing was allowed to float. Both of these possibilities were fit over several energy ranges: 7106−7120, 7107−7120, and 7108−7120 eV. The fit and the second derivative of the fit were compared to the data to determine the quality of a given fit. The areas of the fits were determined using Simpson's rule, which calculates the area by extrapolating to a third data point to fit a quadratic equation (area = $(y_1 + 4y_2 + y_3)\cdot(x_2 - x_1)/6$, where y is the intensity and x is the energy).[13] For the Simpson's rule method, the features of the fit were integrated from 7100 to 7150 eV. The areas and positions for all acceptable fits were averaged, and standard deviations of these averages are reported in parentheses. The V2C XES data were fit and analyzed in a manner similar to the XAS pre-edges analysis, as described above.

Computational Details. All calculations were performed with the ORCA 2.7.0 electronic structure program package developed by Neese and co-workers.[29] Cartesian coordinates for complexes $[L^{tBu}Fe(SPh)(X)]$ (**1**−**4**) were obtained from reported[26] crystal structures, and coordinates for hypothetical complexes were generated by modifying the appropriate crystallographic coordinates of known structure. Geometry optimizations were performed using the BP86 functional,[30,31] in combination with the def2-TZVP(-f) basis set and the def2-TZVP/J auxiliary basis set.[32] Scalar relativistic effects were introduced using the zeroth-order regular approximation (ZORA).[33] The negative charges on the complexes were compensated with the conductor like screening model (COSMO) in an infinite dielectric.[34] All the calculations used a dense integration grid (ORCA Grid 4) with the total energy convergence tolerances of 10^{-6} E_h within tight optimization criteria. For complexes **1**−**4**, the geometry-optimized structures reproduced the experimental X-ray structures with an rms deviation of 0.547, 0.714, 0.593, and 0.289 Å, respectively, by matching all the atoms. The rms deviation reduced to 0.065, 0.118, 0.053, and 0.053 Å, respectively, by comparing [FeN2SX] core atoms. This indicates that only organic substituents are altered significantly in optimized structures. The top portion of Table 1 summarizes the crystallographic and geometry optimized bond lengths for **1**−**4**. Optimizations of hypothetical complexes were performed with the same computational protocol used for model complexes **1**−**4**. Chimera was used for the visualization of molecular orbital contour plots.[35] Quantitative analyses of ORCA outputs were aided by the use of MOAnalyzer.[36] Example ORCA input files for geometry optimizations, and XAS and XES calculations are presented in the Supporting Information.

XAS and XES Calculations. All XAS and XES calculations were performed using optimized geometry. TDDFT calculations were performed to calculated XAS spectra, using the BP86 functional,[30,31] in combination with the def2-TZVP(-f) basis set and the def2-TZVP/J auxiliary basis set. Scalar relativistic effects were introduced using the zeroth-order regular approximation (ZORA). XES spectra were calculated using a simplified one-electron model based on the ground state DFT calculations, utilizing the BP86 functional[30,31] in combination with the CP(PPP) basis set[38] on Fe (with a special integration accuracy of 7) and the TZVP basis set on all remaining atoms. In both the calculations, solvation was modeled using COSMO in an infinite dielectric.[34] Calculated XAS spectra were plotted by applying a 1.5 eV broadening and a constant energy shift of +53.9 eV, while V2C XES spectra were plotted with a 2.5 eV spectral width and an energy shift of +182.5 eV to facilitate comparisons with experiment. XAS pre-edge areas were predicted based on a published TDDFT calibration study on iron complexes.[13] V2C XES areas were predicted based on compounds **1**−**4** and a previously studied[15] set of model compounds' (11 compounds) experimental V2C area and calculated oscillator strength linear relationship, $y = (0.112 \times 10^4)x - 2.278$ (R = 0.92), where y is the predicted intensity and x is the sum of the calculated oscillator strength (Figure S4 of the Supporting Information).

dx.doi.org/10.1021/ic3021723 | Inorg. Chem. 2013, 52, 6286−6298

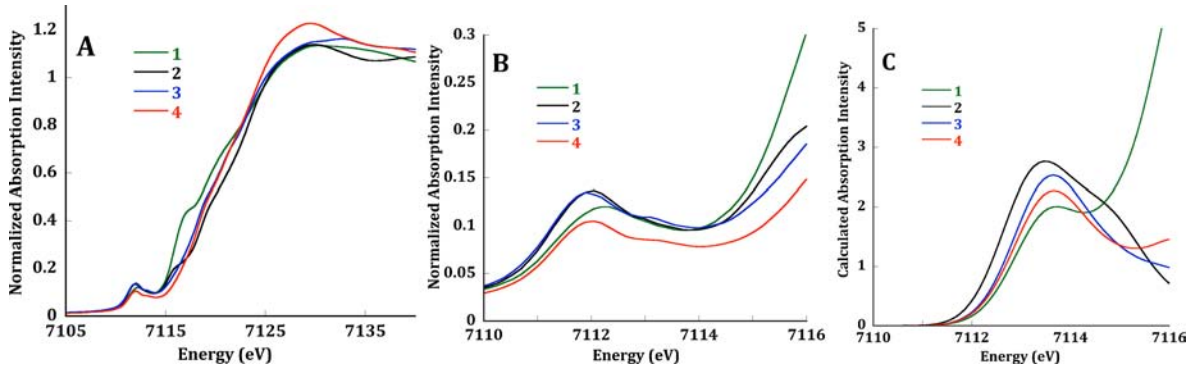

Figure 2. Normalized Fe K-edge XAS spectra for [L^{tBu}Fe(SPh)(X)] (**1**–**4**) (A), and expansion of pre-edge region (B). Calculated Fe K pre-edge XAS for [L^{tBu}Fe(SPh)(X)] (**1**–**4**) (C). A constant energy shift of +53.9 eV and a 1.5 eV broadening have been applied to all calculated XAS spectra.

RESULTS AND ANALYSIS

X-ray Absorption Spectroscopy (XAS). The normalized Fe K-edge XAS spectra of complexes **1**–**4**, and expansion of the pre-edge region are presented in Figure 2, panels A and B. The pre-edge positions and areas are summarized in Table 2. The pre-edge positions for complexes **1**–**4** all appear at ∼7112.2 eV, consistent with a high-spin Fe(II) center in all four complexes.[39] The pre-edge intensity, however, changes over the series, with areas varying from ∼19–28 units of intensity (Table 2). Among the four-coordinate complexes (**2**–**4**), the pre-edge intensity decreases across the series with [L^{tBu}Fe(SPh)(CN^{t}Bu)] (**2**) > [L^{tBu}Fe(SPh)(MeIm)] (**3**) > [L^{tBu}Fe(SPh)(DMF)] (**4**). This trend is consistent with the decrease in covalency of the fourth coordination site (Fe–X bond distance in Table 1).

Table 2. Comparison of Experimental and Calculated Fe K XAS Pre-edge Positions and Areas for [L^{tBu}Fe(SPh)(X)] (1–4)

	pre-edge energy (eV)		pre-edge area	
compd	exptl[a]	calcd[b]	exptl[c]	calcd[d]
1	7112.2	7112.2	23.4	23.9
2	7112.2	7112.1	28.3	31.4
3	7112.2	7112.2	23.5	27.9
4	7112.2	7112.2	18.9	26.5

[a]Intensity weighted average energies. [b]A +53.9 eV constant energy shift has been applied to all calculated energies. [c]Reported pre-edge areas have been multiplied by 100, after normalizing the postedge to 1.0. [d]Calculated pre-edge areas have been determined using experimental areas vs the calculated oscillator strength linear fit line, $y = (1.573 \times 10^5)x + 6.702$ ($R = 0.98$), where y is the predicted area and x is the sum of the calculated oscillator strengths.

In addition to the pre-edge features, complexes [L^{tBu}Fe(SPh)] (**1**) and [L^{tBu}Fe(SPh)(CN^{t}Bu)] (**2**) show intense higher energy features at 7116.7 and 7115.9 eV, respectively (Figure S2 of the Supporting Information). The higher energy feature at 7116.7 eV in three-coordinate complex **1** is tentatively assigned to the Fe 1s → 4p$_y$ transition, where the [N$_2$S] ligand lies in the *xz* plane (Figure 1). Using ligand field considerations, one would predict that 4p$_x$ and 4p$_z$ would be raised in energy relative to 4p$_y$ due to antibonding interactions within the *xz* plane, while 4p$_y$ would be moved to lower energy. Similar trends have been observed previously for copper complexes and verified through polarized single crystal measurements.[40,41] Thus, for complex **1**, the intense (59.9 units) feature at 7116.7 eV on the rising edge is attributed to a low-lying 1s → 4p$_y$ dipole-allowed transition. The higher energy feature (at ∼7115.9 eV with 22.3 units of intensity) in complex **2** is attributed to a transition from Fe 1s to π^* of the isocyanide ligand. Generally, for metal complexes containing π-acceptor ligands, the ligand π^* molecular orbitals are below the metal 4p orbitals, which favors the Fe 1s to ligand π^* transition.[42,43] The assignments of these transitions are further discussed in the computational section.

XAS Calculations. In order to obtain further insight into the XAS spectra of [L^{tBu}Fe(SPh)(X)] (**1**–**4**), the experimental spectra were supplemented with DFT calculations. A time-dependent density functional theory (TDDFT) approach was used for the XAS calculations.[44,13] The calculated Fe K-edge XAS pre-edge spectra for complexes **1**–**4** are presented in Figure 2C, and calculated and experimental pre-edge energies and intensities are summarized in Table 2. Comparison of the experimental and calculated XAS spectra (Figure 2B and C, respectively) and the pre-edge energies and intensities (Table 2) illustrates that the 7110–7116 eV regions are reasonably well-reproduced by the TDDFT calculation.

Analysis of calculated Fe K-edge XAS spectra for complexes **1**–**4** shows that the pre-edge features arise from Fe 1s → Fe 3d(β) transitions to d$_{yz}$, d$_{xz}$, d$_{x^2-y^2}$, and d$_{z^2}$ molecular orbitals (Figure 3). The Löwdin reduced orbital population analysis of complexes **2** and **3** shows that the total Fe 4p character mixed into the 3d orbitals is greatest for **2** (14%) and decreases slightly in **3** (12%) and **4** (11%). These values are consistent

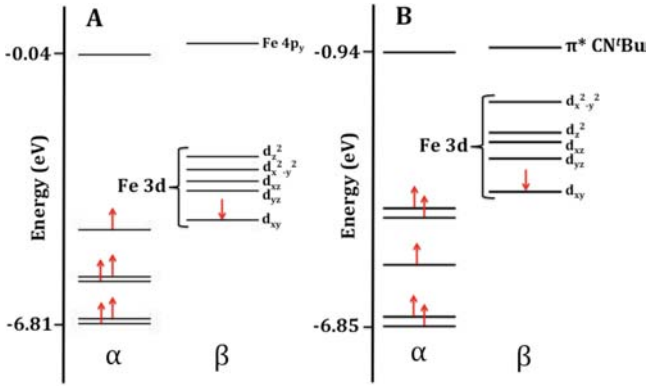

Figure 3. Frontier molecular orbital diagram for [FeL^{tBu}(SPh)] (**1**) (A) and [FeL^{tBu}(SPh)(CN^{t}Bu)] (**2**) (B). Note that the orbital designations for the Fe-based α orbitals follow the same order as the β orbitals.

dx.doi.org/10.1021/ic3021723 | Inorg. Chem. 2013, 52, 6286–6298

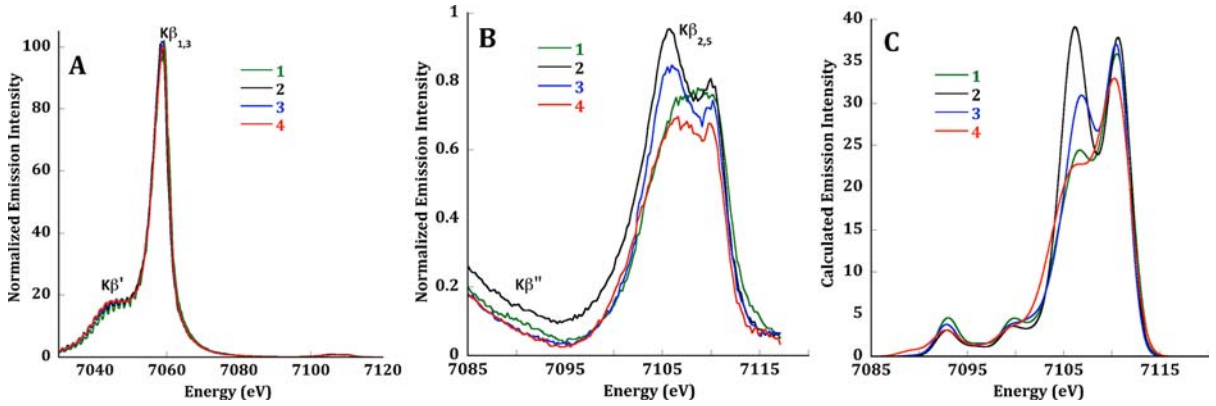

Figure 4. Fe Kβ XES for [L^{tBu}Fe(SPh)(X)] (**1**–**4**) (A). Expansion of the valence to core (V2C) region (B). Calculated Fe Kβ valence to core XES spectra for [L^{tBu}Fe(SPh)X] (**1**–**4**) (C). A constant shift of +182.5 eV and a 2.5 eV broadening have been applied to all calculated XES spectra.

Table 3. Experimental K$\beta_{1,3}$ Maxima, V2C XES Peak Positions, and Areas for [L^{tBu}Fe(SPh)(X)] (1–4)

		V2C XES								
	K$\beta_{1,3}$ max	peak 1		peak 2		peak 3		peak 4		
compd	*E* (eV)	*E* (eV)	area[b]	*E* (eV)	area	*E* (eV)	area	*E* (eV)	area	tot V2C area
1[a]	7058.5	7102.2	2.1	7104.7	1.7	7107.2	2.4	7110.3	3.0	7.8(0.1)
2	7058.2	7101.2	0.9	7104.5	2.3	7106.6	2.5	7110.0	2.9	8.6(0.1)
3	7058.3	7102.1	0.7	7104.7	1.6	7107.0	2.3	7110.2	2.6	7.9(0.1)
4	7058.3	7101.7	0.9	7104.6	1.8	7107.0	2.0	7110.1	2.3	7.0(0.1)

[a]Also exhibits weak satellite feature at 7090.2 eV (1.5 intensity area). [b]Reported areas are out of 1000 units of Kβ XES spectral intensity.

with the decrease in experimental pre-edge intensities across this series. The higher energy "rising" edge features observed in **1** and **2**, at ~7117 and 7116 eV, respectively, are clearly reproduced in the calculations. As suggested above, on the basis of a simple ligand field (LF) model, TDDFT calculation confirms that the ~7117 eV feature in complex **1** corresponds to a dipole-allowed Fe 1s to 4p$_y$ transition. In complex **2**, on the other hand, the higher energy feature arises from Fe 1s to CN^{t}Bu π^* orbitals. However, we note that the calculated energy splitting between the pre-edge and higher energy features is ~2 eV smaller in calculated spectra as compared to the experimental values. Studies by Römelt et al. have shown that the energies of such charge transfer features are strongly basis set dependent.[42,45,46]

X-ray Emission Spectroscopy (XES). The normalized Fe Kβ XES spectra at the Kβ main line (denoted as Kβ'/K$\beta_{1,3}$) and expansion of the valence to core region (denoted as Kβ''/K$\beta_{2,5}$) for complexes **1**–**4** are depicted in Figure 4. The numerical details, including peak positions and intensities for **1**–**4**, are summarized in Table 3.

The Kβ main line is split into two major features: the Kβ' (which corresponds to the weak shoulder at ~7045 eV) and a more intense K$\beta_{1,3}$ emission line (at ~7060 eV). The splitting of these features is primarily due to the 3p–3d exchange interaction, with smaller contributions from spin orbit coupling of the 3p hole state. Hence, the Kβ' feature is well-resolved in the high-spin complexes, whereas in low-spin complexes the Kβ' and K$\beta_{1,3}$ lines merge together to give a single intense Kβ main line.[15,19,47] Complexes **1**–**4** all show a pronounced Kβ' feature at ~7045 eV, similar to reported high-spin ferrous/ferric complexes.[15] The K$\beta_{1,3}$ main line maxima for complexes **1**–**4** appear at ~7058.3 ± 0.1 eV for all four complexes, again consistent with a high-spin ferrous assignment. We note that the 7040–7050 eV region of the Kβ main line exhibits a high-frequency structure, which is attributed to instrumental vibrations at the low-energy limit of the spectrometer. However, these features do not change the general interpretation of the observed spectra.

The V2C XES region for complexes **1**–**4** shows more pronounced differences across the series than the main line region, as can be seen in Figure 4B. The K$\beta_{2,5}$ region (at ~7100–7115 eV) corresponds primarily to ligand 2p (C, N, O) or 3p (S) to Fe 1s transitions, which gain intensity through a small amount of Fe 4p mixing into these orbitals.[20] As the fourth ligand is varied, there are changes in both the splitting of the K$\beta_{2,5}$ features and the intensities, as indicated in Table 3. The total integrated V2C XES area for complexes **1**–**4** ranges from 7 to 9 units of normalized intensity; these areas are relatively different beyond the 10% normalization error associate with the V2C area.[15,48] The observed V2C areas for **1**–**4** are consistent with the reported[15] high-spin Fe(II) complexes. Previous studies[15,49] have shown that the intensity of the V2C XES spectra depends strongly on metal–ligand bond distances, with the intensity falling off exponentially with increasing M–L bond distance.

The Kβ'' features are assigned to ligand 2s (C, N, O) or 3s (S) transitions to the metal 1s hole, which gain intensity through small amounts of Fe *n*p mixing into the ligand *n*s orbitals. In the current series, only complex **1** exhibits a (very weak) Kβ'' feature at ~7090.2 eV (Figure S3 of the Supporting Information), while complexes **2**–**4** do not exhibit any clear Kβ'' features. This indicates that the ligand 2s to metal 1s transitions are too weak to be observed in these complexes and/or are buried in the tail of the Kβ main line. This may be a result of delocalization of the ligand 2s character over the entire ligand framework, resulting in a decrease in intensity. This observation is further explored in the computational section.

dx.doi.org/10.1021/ic3021723 | *Inorg. Chem.* 2013, 52, 6286–6298

Table 4. Calculated V2C Kβ XES Feature Positions and Areas for [L^{tBu}Fe(SPh)(X)] (1−4)

	calcd Kβ″ features				calcd $Kβ_{2,5}$ features				
compd	E (eV)[b]	area	E (eV)	area	E (eV)	area	E (eV)	area	tot calcd V2C area[a]
1	7093.4	0.47	7099.3	0.44	7105.4	2.93	7110.1	4.48	8.3
2	7093.3	0.34	7099.9	0.51	7106.1	4.87	7110.5	3.80	9.5
3	7093.1	0.39	7100.1	0.68	7106.2	3.78	7110.1	3.78	8.6
4	7092.5	0.44	7099.8	0.54	7105.1	2.75	7109.8	4.54	8.3
Assignments	N_{imine} 2s → Fe 1s		S 3s → Fe 1s		S σ 3p → Fe 1s N_{imine} σ 2p → Fe 1s X σ 2p → Fe 1s		S σ* 3p → Fe 1s N_{imine} σ* 2p → Fe 1s X σ* 2p → Fe 1s Fe 3d → Fe 1s		

[a]Calculated V2C XES areas predicted using experimental areas vs the sum of the calculated XES oscillator intensities linear fit line, $y = (0.112 \times 10^4)x - 2.278$ ($R = 0.92$), where y is the predicted area and x is the sum of the calculated oscillator strengths. [b]+182.5 eV constant energy shift applied to all calculated XES energies.

XES Calculations. The calculated valence to core XES spectrum for **1**−**4** is depicted in Figure 4C. Comparing the calculated spectra with the experimental valence to core region of the Fe Kβ XES of complexes **1**−**4** (Figure 4B) shows that a simple one-electron DFT model reproduces all experimental spectral features. The experimental V2C areas and sum of the calculated oscillator strengths are found to vary linearly (Figure S4 of the Supporting Information) with $R = 0.92$. Using the above linear correlation, V2C areas were obtained and presented in Table 4. The calculated XES spectra for complexes **1**−**4** exhibit four distinct features in the valence to core region: a weak satellite at ∼7093 eV, a second satellite at ∼7100 eV, and two intense $Kβ_{2,5}$ features at ∼7106 and ∼7111 eV.

A low-energy and low-intensity satellite feature or "crossover feature" (Kβ″) is observed at ∼7093.1 eV for all four complexes, and it has slightly more intensity for the three-coordinate complex **1**. This feature arises from a transition from the N 2s orbitals of β-diketiminate ligand to the metal 1s core hole. The V2C XES spectra intensity directly correlates with metal−ligand bond distances, and in the case of complex **1**, the Fe−N distance is slightly shorter (0.1 Å) than the analogous bonds present in **2**−**4** (see Table 1), resulting in a slightly more intense feature. We note that this feature is observed experimentally only for complex **1** as a broad feature at 7090.2 eV, as shown in pseudo-Voigt deconvoluted V2C spectra (Figure S3 of the Supporting Information).

In addition, all calculated V2C XES spectra show a weak Kβ″ feature at ∼7100 eV, which originates from a transition from the sulfur 3s orbitals of the phenyl thiolate to the Fe 1s hole. This feature is correlated with the weak shoulder which appears experimentally between 7101 and 7102 eV in all four complexes. As this feature is poorly resolved, direct correlation of experimental and calculated intensities is difficult to assess. In general, the intense Kβ″ feature arises from molecular orbitals with dominantly ligand 2s or 3s antibonding (σ*) character, rather than the bonding (σ) orbitals, which may be attributed to the better overlap between ligand *n*s antibonding orbitals and the Fe *n*p orbitals. For instance, in complex **1**, the N_{imine} 2s bonding orbital has 2% of Fe p character, compared to 3% Fe p character in the antibonding N_{imine} 2s orbital.

The intense feature centered around 7106 eV shows more variations in intensity between complexes **1**−**4**. These $Kβ_{2,5}$ features are attributed to a combination of transitions from ligand (both N_{imine} and heteroatom) 2p and sulfur 3p bonding (σ) orbitals to the Fe 1s orbital. In addition to the above intensity mechanism, complexes **2** and **3** gain additional intensity due to interaction of Fe 4p orbitals with $σ^*_{2s\text{-}2s}$ and $σ_{2p\text{-}2p}$ orbitals of π-acidic isocyanide and imidazole ligands, respectively. Iron complexes containing π-acidic ligands, such as CN^- and CO, show intense low-energy $Kβ_{2,5}$ features in this energy range due to metal 4p mixing into the 2s−2s antibonding orbital of the CO and CN ligands. Thus, complex **2**, which contains the strong π-acidic ligand *tert*-butyl isocyanide coordinated to the Fe(II) center, shows the most intense (4.43 units) feature in this region (Table 4). Hence, this region of the spectrum provides a useful marker for the identity of the fourth ligand in this series.

The highest energy $Kβ_{2,5}$ feature (at ∼7110 eV) for all four complexes results from contributions from the antibonding (σ*) *n*p orbitals of S (thiolate), N (imine), and X (heteroatom) donors. In all cases, there is significant Fe 4p character mixed into the MOs (∼2−6% Fe 4p), giving these transitions dipole-allowed intensity. In the case of complex **1**, the primary contributions to the ∼7110 eV feature arise from antibonding S 3p (24% S p, 8% Fe d, 5% Fe p) and N 2p (19% N p, 29% Fe d, 5% Fe p) molecular orbitals with a substantial amount of Fe p character. In complex **2**, the contributions to the 7110 eV features are dominated by S 3p (36% S p, 27% Fe d, 6% Fe p), N 2p (20% N p, 24% Fe d, 5% Fe p), and C 2p (3% C p, 20% Fe d, 2% Fe p). Similar trends are observed for **3** and **4**. Hence, for the four-coordinate complexes, the contributions to the ∼7110 eV feature follow the order X 2p < N_{imine} 2p < S 3p, indicating that the fourth ligand makes the smallest contribution to the observed intensity in this energy region.

Calculations on Hypothetical Iron Complexes. Having established the correlation between the experimental and calculated spectra for model complexes **1**−**4**, we now extended our computational studies to a series of hypothetical complexes, in which the protonation state, oxidation state, and ligand environments at the high-spin iron centers were systematically varied. These changes are vital steps in transition-metal-mediated catalysis; for example, iron species bound to nitrogen based ligands in various protonation states are proposed intermediates in both surface[50] (Haber−Bosch process) and biological[51,52] (nitrogenase) catalyzed synthesis of ammonia from dinitrogen. Similarly, high-valent iron oxo species are well-known intermediates in several oxygenase family enzymes.[53,54] To understand the relative sensitivity of XAS and XES spectroscopic techniques, sets of catalytically relevant complexes were geometry optimized and spectral calculations were performed at the same level of theory as utilized for **1**−**4**. The same broadening was applied to all calculated spectra (1.5 eV for XAS and 2.5 eV for XES) to allow for a reasonable assessment of what one should be able to observe

dx.doi.org/10.1021/ic3021723 | Inorg. Chem. 2013, 52, 6286−6298

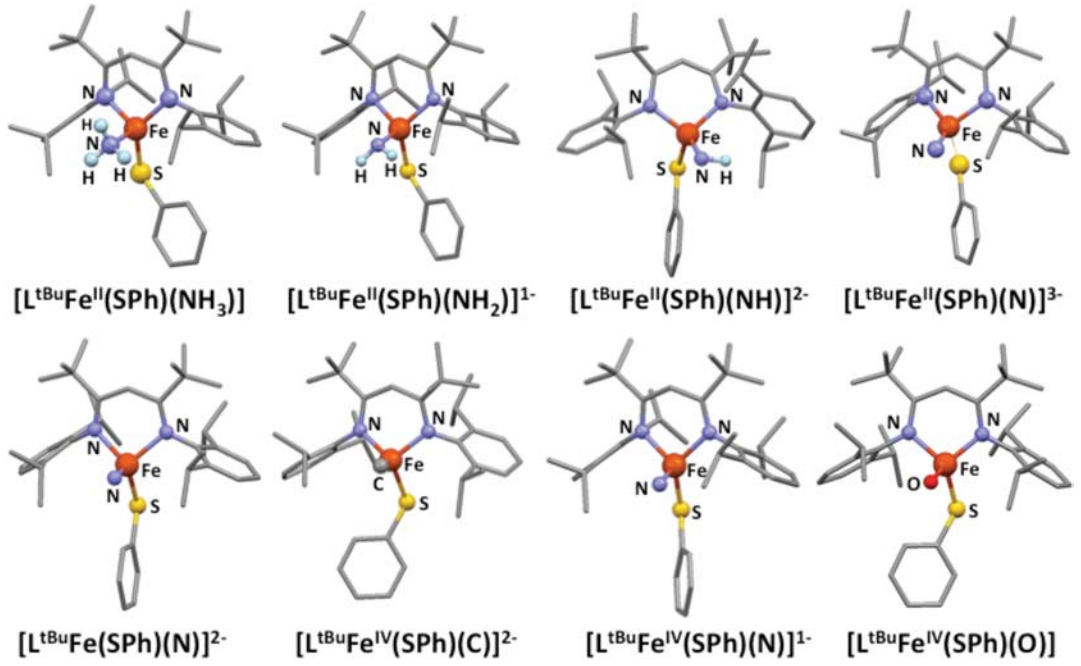

Figure 5. Optimized structures of hypothetical Fe complexes. Hydrogen atoms are omitted for clarity except for the terminal X ligand. The $[N_2S]$ ligand frame for all the complexes lies within the *xz* plane, whereas the fourth terminal ligand lies along the *y* axis.

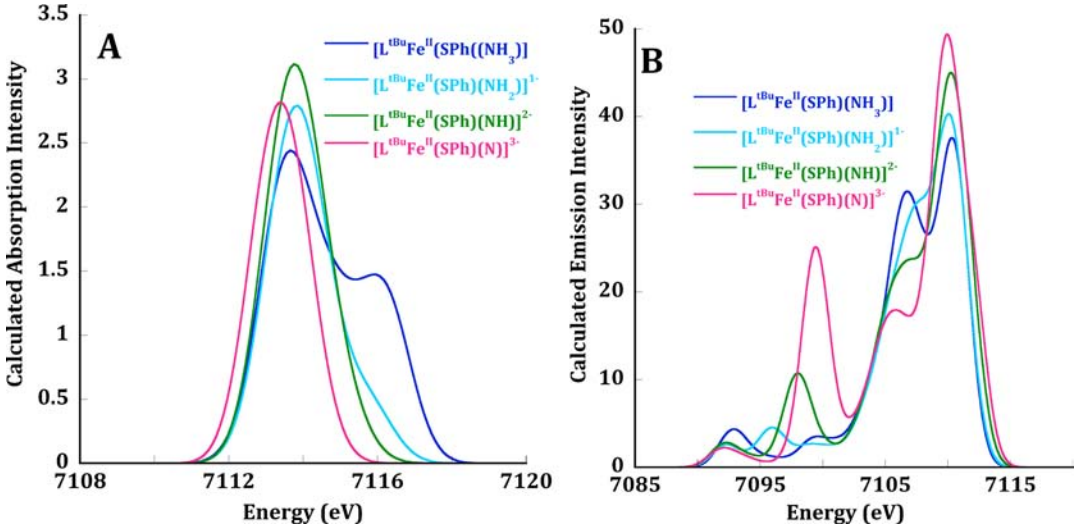

Figure 6. Calculated Fe K pre-edge XAS (A) and Fe Kβ valence to core XES (B) spectra for $[L^{tBu}Fe^{II}(SPh)(NH_n)]^{3-n}$ (n = 3, 2, 1, 0). A constant shift of +53.9 eV and a 1.5 eV broadening have been applied to all calculated XAS spectra; a +182.5 eV energy shift and a 2.5 eV broadening have been used for all calculated XES spectra.

experimentally. We note that in some cases weak features, such as the Kβ'' feature, may be too weak to be observed and/or obscured by the background (i.e., the rising edge or the tail of the Kβ main line). These cases are noted throughout. The optimized structures are presented in Figure 5; the important bond distances and geometry index (τ_4) for all the optimized hypothetical molecules are also summarized in Table 1.

Effect of Protonation State. Calculated X-ray absorption and emission spectra for $[L^{tBu}Fe^{II}(SPh)(NH_n)]^{3-n}$ (n = 3, 2, 1, 0), where the protonation of the terminal nitrogen ligand is varied from NH_3 to N, were investigated. We note that while Fe(II)-imido or -nitrido complexes are unlikely, this hypothetical series allows us to systematically test the effect of a ligand protonation/deprotonation without changing Z_{eff} on the metal. Across the series, the terminal Fe−N bond distance gradually shortens from 2.152 Å (in $[L^{tBu}Fe^{II}(SPh)(NH_3)]$) to 1.679 Å for the Fe(II) nitrido species $[L^{tBu}Fe^{II}(SPh)(N)]^{3-}$. The opposite trend is observed for the Fe−S bond, which is elongated upon successive deprotonation steps, due to increased donation from the nitrogen ligand (Table 1). At the limit of $[L^{tBu}Fe^{II}(SPh)(N)]^{3-}$, the Fe−S bond distance increases to 2.611 Å, which is slightly longer than the sum of covalent radii for Fe and S (2.54 Å). The Fe−N(β-diketiminate) bond distances remain almost identical for all members of the $[L^{tBu}Fe^{II}(SPh)(NH_n)]^{3-n}$ series. The optimized geometries for this series of hypothetical complexes may be described as lying between the limits of tetrahedral and trigonal pyramidal geometries. Although several methods are available

dx.doi.org/10.1021/ic3021723 | Inorg. Chem. 2013, 52, 6286−6298

for the quantitative geometric description of four-coordinate complexes,[55−57] we have chosen to use the geometry index (τ_4), as reported by Houser et al.[37] For idealized tetrahedral and square planar geometries, the τ_4 values are 1 and 0, respectively, whereas perfect trigonal pyramidal complexes have a τ_4 value of 0.85. As indicated in Table 1, the complex $[L^{tBu}Fe^{II}(SPh)(NH_3)]$ (τ_4 = 0.84) is close to a trigonal pyramidal geometry and moves toward tetrahedral geometry with deprotonation of the terminal nitrogen ligand. In the case of the Fe(II) nitrido complex, τ_4 is 0.75, due to a greater distortion from trigonal pyramidal geometry.

The Fe K pre-edges of this hypothetical series are shown in Figure 6A, and the calculated pre-edge energies and intensities are summarized in Table 5. The calculated intensities span a range of 28−41 units (referenced to 100 units of normalized Fe K-edge intensity), with the lowest and highest intensities observed for $[L^{tBu}Fe^{II}(SPh)(NH_3)]$ and $[L^{tBu}Fe^{II}(SPh)(NH)]^{2-}$, respectively. From $[L^{tBu}Fe^{II}(SPh)(NH_3)]$ to $[L^{tBu}Fe^{II}(SPh)(NH)]^{2-}$, steady increases in pre-edge intensity were observed, due to better overlap between the terminal NH_n^{3-n} ligand and the Fe center (i.e., increasing covalency), which mediates the Fe 3d−4p mixing.[58] However, the Fe(II) nitrido complex $[L^{tBu}Fe^{II}(SPh)(N)]^{3-}$ deviates from the observed trend, despite having a very short Fe−N bond distance, and the pre-edge intensity is 4 units lower than the $[L^{tBu}Fe^{II}(SPh)(NH)]^{2-}$. This deviation in the trend suggests the absence of thiolate mediated 3d−4p mixing in the Fe(II)-nitrido species, while in the other test compounds 3d−4p mixing is mediated by both the terminal nitrogen and the ancillary thiolate ligand. Across the series, the pre-edge energy peak maxima remain very similar at 7112.5 ± 0.2 eV. This indicates a comparable effective charge on the iron in this series and a similar average ligand field—suggesting a strong spectator effect in which the ancillary ligands (SPh) compensate for changes in the nitrogen ligand donation.

Table 5. Calculated Fe K XAS Pre-edge Positions and Areas for Hypothetical Fe Complexes

compd	calcd pre-edge energy (eV)[a]	calcd pre-edge area[b]
$[L^{tBu}Fe(SPh)(NH_3)]$	7112.2	27.7
$[L^{tBu}Fe(SPh)(NH_2)]^-$	7112.5	37.5
$[L^{tBu}Fe(SPh)(NH)]^{2-}$	7112.5	40.7
$[L^{tBu}Fe(SPh)(N)]^{3-}$	7112.1	37.8
$[L^{tBu}Fe(SPh)(N)]^{2-}$	7112.4	43.7
$[L^{tBu}Fe(SPh)(C)]^{2-}$	7112.9	70.6
$[L^{tBu}Fe(SPh)(N)]^-$	7112.6	87.7
$[L^{tBu}Fe(SPh)(O)]$	7112.8	53.5

[a]A +53.9 eV constant energy shift has been applied to calculated energies. [b]Calculated pre-edge areas have been determined using experimental areas vs the calculated oscillator strength linear fit line, $y = (1.573 \times 10^5)x + 6.702$ ($R = 0.98$), where y is the predicted area and x is the sum of the calculated oscillator strengths.

In contrast to the calculated XAS spectra, the calculated XES spectra show far greater sensitivity to changes in protonation state on the ligand, as shown in Figure 6B. The calculated spectra clearly show two Kβ'' features (~7092.5 and ~7094.1−7099.5 eV) and two K$\beta_{2,5}$ features (~7105.5 eV and ~7110.3 eV). The lowest energy Kβ'' feature at ~7092.5 eV corresponds to the transition from the 2s orbitals of the β-diketiminate N, and it does not show significant changes over the series, consistent with the fact that the Fe−N(β-diketiminate) distances do not vary considerably. The higher energy Kβ'' features in the 7094.1−7099.5 eV region (corresponding to transitions from the 2s orbitals of the terminal NH_n^{3-n} ligand to the metal 1s core) show pronounced changes in both energy and intensity (Table 6). From Fe-NH_3 to Fe−N^{3-}, the bond length decreases by 0.5 Å, providing a mechanism for the dramatic increase in the intensity of this feature upon deprotonation. The bond length and XES Kβ'' (X 2s) intensity have an exponential relationship (Figure 7A), consistent with previous observations.[15,49] The Kβ'' intensity typically varies linearly with the percent Fe p character (Figure 7B).[20] The above observation is consistent with the metal 4p mixing decreasing exponentially as the metal−ligand bond lengths increase. This is an important observation, as it indicates that, at longer metal−ligand bond lengths, the Kβ'' features will become too weak to be experimentally observed. In addition to the change in intensities, the energies also shift by ~5 eV from NH_3 to N^{3-}, reflecting the changes in the 2s ionization potential of the terminal NH_n^{3-n} ligand. We note that an additional weak feature occurs at ~7100.3 eV, which is attributed to the S 3s → Fe 1s transition. The S 3s → Fe 1s Kβ'' feature loses intensity as the Fe−S bond is elongated, due

Table 6. Calculated V2C Kβ XES Positions and Areas for Hypothetical Fe Complexes

		calcd Kβ'' features				calcd K$\beta_{2,5}$ features			
compd	predicted tot V2C intensity[a]	E (eV)[b]	area	E (eV)	area	E (eV)	area	E (eV)	area
$[L^{tBu}Fe(SPh)(NH_3)]$	8.6	7092.6	0.26	7094.1	0.19	7105.4	4.42[c]	7110.3	3.70
$[L^{tBu}Fe(SPh)(NH_2)]^-$	8.8	7092.4	0.23	7096.0	0.41	7105.8	4.20	7110.3	3.97
$[L^{tBu}Fe(SPh)(NH)]^{2-}$	9.9	7092.7	0.32	7098.3	1.11	7105.7	3.18	7110.3	5.32
$[L^{tBu}Fe(SPh)(N)]^{3-}$	11.5	7092.6	0.27	7099.5	2.44	7105.0	1.99	7110.1	6.79
$[L^{tBu}Fe(SPh)(N)]^{2-}$	9.9	7092.2	0.18	7100.2	2.02	7105.8	2.34	7110.7	5.35
$[L^{tBu}Fe(SPh)(C)]^{2-}$	12.6	7094.0	0.35	7103.3	3.61	7106.5	2.26	7111.0	6.38
$[L^{tBu}Fe(SPh)(N)]^-$	11.4	7093.0	0.28	7099.9	2.95	7105.6	2.57	7110.0	5.62
$[L^{tBu}Fe(SPh)(O)]$	13.7	7093.7	0.32	7095.6	2.39	7105.5	3.58[c]	7110.4	7.40
Assignments		N_{imine} 2s → Fe 1s		X 2s → Fe 1s		S σ 3p → Fe 1s N_{imine} σ 2p → Fe 1s X σ 2p → Fe 1s		S σ^* 3p → Fe 1s N_{imine} σ^* 2p → Fe 1s X σ^* 2p → Fe 1s Fe 3d → Fe 1s	

[a]Predicted V2C XES areas have been determined on the basis of the linear fit line, $y = (0.112 \times 10^4)x - 2.278$ ($R = 0.92$), where y is the predicted area and x is the sum of the calculated oscillators strengths. [b]A +182.5 eV constant energy shift has been applied to all calculated XES energies. [c]Includes the contribution from S 3s → Fe 1s (which appears at 7100.3 eV).

dx.doi.org/10.1021/ic3021723 | Inorg. Chem. 2013, 52, 6286−6298

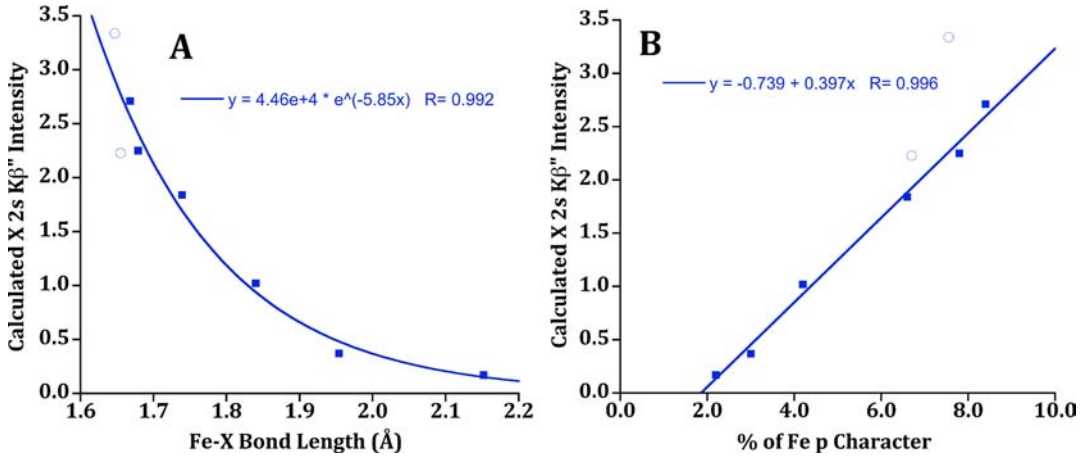

Figure 7. Relationship between calculated X 2s Kβ'' intensity and Fe−X bond length (A), and percent of Fe 4p character (B) for hypothetical complexes presented in Table 6. Solid squares correspond to X = NH_n; open circles are for X = C or O. Fits are based only on the X = NH_n series.

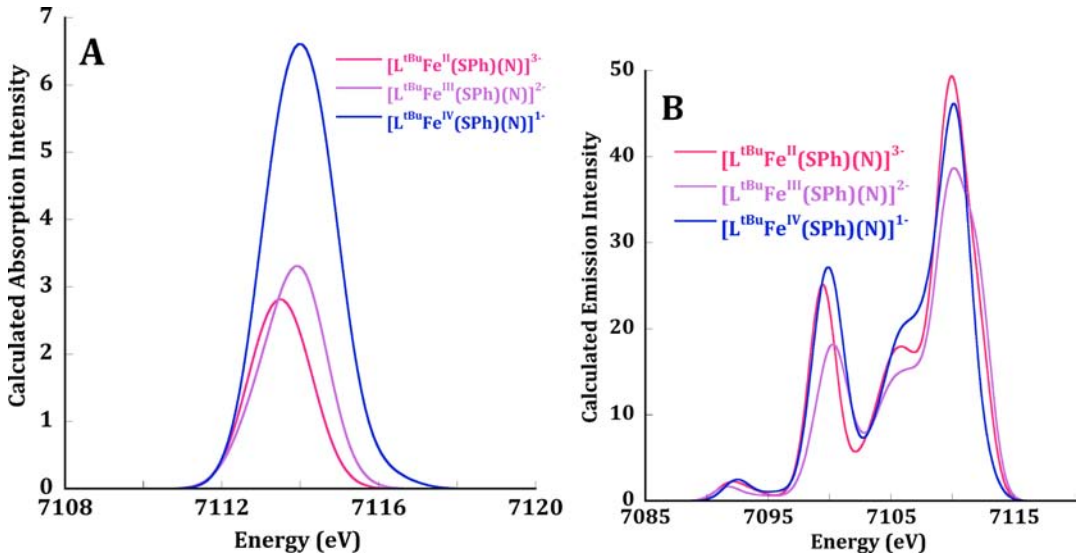

Figure 8. Calculated Fe K pre-edge XAS (A) and Fe Kβ valence to core XES (B) spectra for $[L^{tBu}Fe(SPh)(N)]^{n-}$ (n = 3, 2, 1). A constant shift of +53.9 eV and a 1.5 eV broadening have been applied to all calculated XAS spectra, whereas a +182.5 eV energy shift and a 2.5 eV broadening have been used for all calculated XES spectra.

to a loss of metal−ligand overlap; however, the position remains unaffected because the Kβ'' position relates to the ionization potential of the ligand.

Intensity changes are observed for the two K$\beta_{2,5}$ features at 7105.5 and 7110.3 eV in the calculated V2C XES spectra of the $[L^{tBu}Fe^{II}(SPh)(NH_n)]^{3-n}$ series. The lower energy and lower intensity K$\beta_{2,5}$ feature observed at 7105.5 eV originates from ligand (N, S, and X) bonding (σ) $np \rightarrow$ Fe 1s core hole filling events, with the S 3p bonding orbitals of coordinated phenyl thiolate being the primary contributor to this feature. Hence, the low-energy K$\beta_{2,5}$ feature intensity decreases upon successive proton removal from the terminal NH_3 ligand due to the coupled elongation of the Fe−S bond, rather than from a direct contribution from the terminal NH_n. In contrast, the higher energy K$\beta_{2,5}$ features observed at ∼7110.3 eV for all the complexes are mainly associated with transitions from N 2p-based molecular orbitals mixed with a significant amount of Fe 3d/4p character. Hence, the increase in intensity of this feature directly reflects the shortening of the Fe−N bond upon successive deprotonations (Table 6). The bonding and antibonding N 2p orbitals of the β-diketiminate spectator ligand also contribute to the K$\beta_{2,5}$ intensity, but this contribution remains unchanged along the series.

Effect of Oxidation State. Figure 8 presents the calculated XAS pre-edge and V2C XES spectra for $[L^{tBu}Fe(SPh)(N)]^{n-}$ (n = 3, 2, 1), where the iron oxidation state is varied from Fe(II) to Fe(IV). Noteworthy structural changes are observed, as summarized in Table 1. As discussed previously, in the Fe(II) nitrido complex $[L^{tBu}Fe(SPh)(N)]^{3-}$, the Fe−S(thiolate) is a noncovalent interaction, with the Fe···S bond distance of 2.611 Å. Upon increasing the oxidation state to Fe(III) in $[L^{tBu}Fe(SPh)(N)]^{2-}$, the Fe−S bond distance shortens significantly to 2.395 Å, while the remaining metal ligand distances elongate by 0.05−0.10 Å. Increasing the oxidation state to Fe(IV) decreases the Fe−N(nitride) bond length and the Fe−S(thiolate) bond length, while the Fe−N(β-diketiminate) distances in $[L^{tBu}Fe(SPh)(N)]^{2-}$ elongate slightly. The τ_4 value of the Fe(II)−nitrido complex is 0.75, whereas the similar geometric parameters for Fe(III) and Fe(IV) species are 0.93 and 0.95, respectively. These values indicate that the increase in oxidation state on iron is coupled to a geometry change from trigonal pyramidal to tetrahedral.

dx.doi.org/10.1021/ic3021723 | Inorg. Chem. 2013, 52, 6286−6298

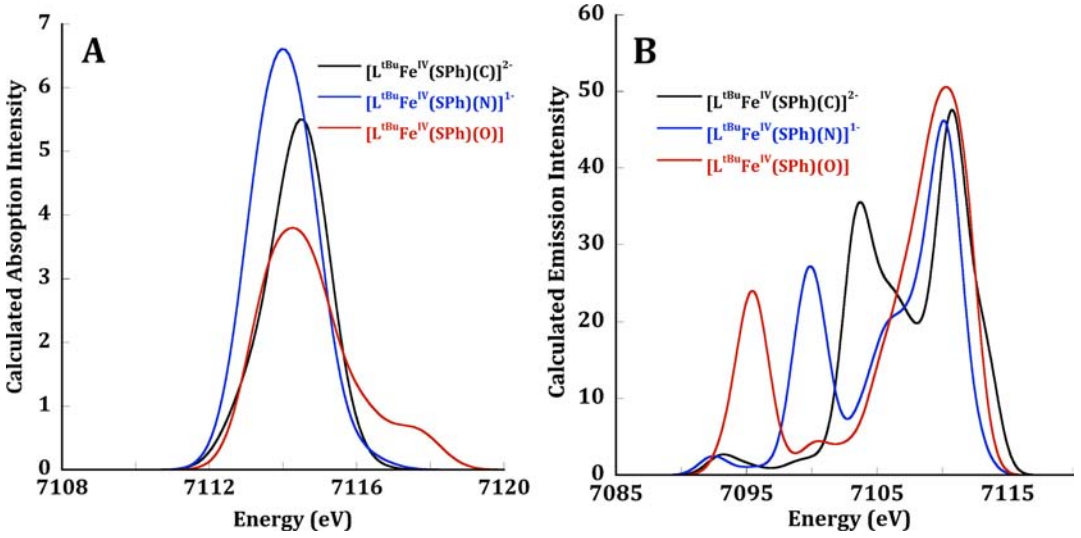

Figure 9. Calculated Fe K pre-edge XAS (A) and Fe Kβ valence to core XES (B) spectra for $[L^{tBu}Fe^{IV}(SPh)(X)]^{n-}$ (X = C^{4-}, N^{3-}, O^{2-}; n = 2, 1, 0). A constant shift of +53.9 eV and a 1.5 eV broadening have been applied to all calculated XAS spectra, whereas a +182.5 eV energy shift and a 2.5 eV broadening have been used for all calculated XES spectra.

Significant variations in both pre-edge intensity and position are observed in the calculated Fe K pre-edge spectra for this set of complexes (Figure 8A and Table 5). A small increase in intensity (by 6 units) is observed on changing the oxidation state from Fe(II) to Fe(III), whereas, upon increasing the oxidation state from Fe(III) to Fe(IV), the pre-edge intensity increases by 44 units (Table 5). This small increase on going from Fe(II) to Fe(III) is consistent with increasing the number of holes in the d-shell, while the more dramatic increase for the Fe(IV) also reflects a significant increase in covalently mediated metal 3d−4p mixing. More specifically, the high pre-edge intensity in the Fe(IV) arises from a unoccupied spin-up Fe d_{xz} (27%) orbital containing 7% Fe p and 36% terminal N p character. In the Fe(II) and Fe(III) complexes, the d_{xz} is occupied, thus decreasing this intensity mechanism. Interestingly, over this series, pre-edge energy only increases by ∼0.3 eV per each change of oxidation state. This effect is smaller than the typical 1 eV per oxidation state[39,59] but likely reflects the significant change in thiolate donation, which partially compensates for the increase in Z_{eff}.

The V2C XES spectra of the $[L^{tBu}Fe(SPh)(N)]^{n-}$ (n = 3, 2, 1) series show more subtle changes than the XAS as the oxidation state is changed (Figure 8B). The calculated spectra show two distinct Kβ'' features: (1) a weak band at ∼7092.5 eV and (2) a more intense feature at ∼7100 eV. These features correspond to N 2s → Fe 1s transitions from the β-diketiminate and terminal nitrido ligands, respectively. The energy difference between these two Kβ'' features corresponds to the difference between the N 2s ionization potentials of the terminal nitrido (N^{3-}) and the β-diketiminate nitrogen. The intensities of these Kβ'' features directly correlate with the Fe−N(nitride) bond distances (Table 1), and thus, the N(nitride) 2s overlap with the Fe p orbitals dominates the spectral intensity. The intensities of the nitrido Kβ'' features follow the trend Fe(III) < Fe(II) < Fe(IV), which directly correlates with the Fe−N(nitride) bond distances (Table 1) and Fe 4p mixing into N 2s MOs (Figure 7B). The position of the Kβ'' features does not vary much upon the changing oxidation state on Fe. This suggests that the change in Z_{eff} at the metal is relatively small (vide supra) and that the ligand ionization potential is the dominant contribution to the Kβ'' energy.[60] All three complexes exhibit a weak $K\beta_{2,5}$ feature around 7105.5 eV and an intense higher energy feature at ∼7110 eV, and these features are consistent with the presence of longer Fe−S and shorter Fe−N bonds in this set of complexes.

Effect of Ligand Environment. To systematically investigate the sensitivity of XAS and XES spectra to changes in the ligand environment, a final set of calculations were carried out on high-spin Fe^{IV} complexes $[L^{tBu}Fe^{IV}(SPh)(X)]^{n-}$ (n = 2, 1, 0), where X was varied from C^{4-} to N^{3-} and O^{2-}. The geometry optimized structures of $[L^{tBu}Fe^{IV}(SPh)(X)]^{n-}$ reveal that $[L^{tBu}Fe^{IV}(SPh)(C)]^{2-}$ has the shortest terminal Fe−X (Fe−C = 1.647 Å) bond and longest Fe−S bond (2.410 Å) in this series (Table 1). The τ_4 value increases from $[L^{tBu}Fe^{IV}(SPh)(O)]$ (0.74) to $[L^{tBu}Fe^{IV}(SPh)(C)]^{2-}$ (0.89) to $[L^{tBu}Fe^{IV}(SPh)(N)]^{-}$ (0.95). This indicates that the Fe(IV)-nitrido complex deviates most from trigonal pyramidal toward tetrahedral geometry.

Calculated Fe K XAS spectra for $[L^{tBu}Fe^{IV}(SPh)(X)]^{n-}$ (X = C^{4-}, N^{3-}, and O^{2-}) are in Figure 9A. Calculated pre-edge positions for these complexes appear at 7112.8 ± 0.2 eV, consistent with a similar Fe oxidation state across this series. The pre-edge intensity varies appreciably for this set of complexes and follows the order $[L^{tBu}Fe^{IV}(SPh)(N)]^{-}$ > $[L^{tBu}Fe^{IV}(SPh)(C)]^{2-}$ > $[L^{tBu}Fe^{IV}(SPh)(O)]$.[61] Interestingly, this does not follow the trend one would expect on the basis of Fe−X bond distances and covalency considerations alone. While the Fe(IV)-carbido might be expected to show an intense pre-edge feature due to greater covalency, the calculated oscillator strength is, in fact, lower. This may indicate that the more tetrahedral geometry of the nitride complex provides a more efficient mechanism for 4p mixing.

The valence to core XES spectra in various ligand environments show larger variations in both energy and intensity compared to XAS pre-edge spectra. The distinct Kβ'' or crossover feature, which corresponds to transitions from the 2s orbitals of the coordinated light atom (C, N, O), shows a pronounced energy change and a systematic variation in intensity. An energy change of ∼8 eV across the series is observed and reflects the inverse relationship with the 2s

dx.doi.org/10.1021/ic3021723 | Inorg. Chem. 2013, 52, 6286−6298

ionization energy of the light atom.[62] The intensity of the Fe-X Kβ″ feature decreases in intensity from C to N to O, reflecting both the decrease in covalency and increase in bond length (Figure 9B). We also note that inclusion of X = C and O to the correlations in Figure 7 slightly decreases the quality of the correlation (with R increasing to 0.97 and 0.95 in parts A and B, respectively, of Figure 7). The V2C spectrum of $[L^{tBu}Fe^{IV}(SPh)(O)]$ exhibits a weak Kβ″ feature at 7100.3 eV, which is due to the S 3s → Fe 1s transition. The above S 3s Kβ″ feature for $[L^{tBu}Fe^{IV}(SPh)(N)]^-$ merges with the terminal N Kβ″ emission line, which also appears at ∼7100 eV. In the case of $[L^{tBu}Fe^{IV}(SPh)(C)]^{2-}$, the S 3s → Fe 1s band is not well-resolved, due to the relatively longer Fe−S bond distance, which decreases the intensity. We also note that previous experimental studies have shown that the calculated 3s intensity is generally overestimated within the one-electron DFT approach employed here, and thus, such features are unlikely to be experimentally observed.[15,25] It is also possible that the Kβ″ feature may be partially obscured by the tail of the Kβ main line in experimental spectra. The contribution of the Kβ main line is not well-calculated in the present approach.

Finally, we note that the Kβ″ corresponding to the Fe−N(diketiminate) feature at ∼7095 is effectively unchanged, consistent with the similar Fe−N(diketiminate) bond lengths in this series. However, due to the low intensity of this feature, it is unlikely to be observed experimentally, consistent with the experimental results reported for complexes **2**−**4**, vide infra, and previous observations for Mn V2C XES.[48]

The $Kβ_{2,5}$ features for these sets of complexes have a low-intensity shoulder around 7105.5 eV and a more intense feature at 7110.5 eV. The low-energy feature intensity increases as the Fe−S bond distance decreases, as this feature primarily originates from S 3p bonding orbitals (Table 6). The higher energy $Kβ_{2,5}$ feature observed at 7110.5 for this set of complexes originates from ligand (C, N, and O) $σ^*_{2p}$ → Fe 1s transitions, as these antibonding ligand orbitals overlap significantly with the Fe 4p/3d orbitals.

SUMMARY AND CONCLUSIONS

XAS and XES are differentially sensitive to changes in the coordination sphere in low-coordinate, high-spin Fe(II) model complexes $[L^{tBu}Fe(SPh)(X)]$. In XAS spectra, the pre-edge position does not change significantly upon the variation of ligation sphere, whereas the pre-edge intensities differ substantially. These trends are reproduced using a TDDFT approach, and they provided quantitative information regarding the degree of metal and ligand interaction (covalency).

The Fe Kβ XES main line features are primarily sensitive to metal spin and oxidation state, with more subtle contributions from coordination number and ligation sphere of the metal. The V2C XES region, on the other hand, exhibits changes in both energy and intensity upon changing the iron ligation environment. The experimental XES V2C spectra were reasonably well-modeled by DFT calculations and formed the basis for a broader investigation of the effects of ligand protonation state, metal oxidation state, and ligand identity on hypothetical complexes.

The following conclusions can be derived from our systematic XAS pre-edge and V2C XES assessment:

(1) The XAS pre-edge positions do not change drastically (no more than ∼0.2 eV) upon altering the protonation state on the terminal nitrogen ligand in the $[L^{tBu}Fe^{II}(SPh)(NH_n)]^{3-n}$ (n = 3, 2, 1, 0) series. A XES Kβ″ feature originating from the 2s orbital of the terminal nitrogen ligand steadily increases in intensity (by a factor of ∼2) and energy (by ∼2.4 eV) upon each deprotonation event. Thus, the V2C XES is a superior spectroscopic technique for identifying the ligand protonation state.

(2) Comparison of calculated XAS and XES features on $[L^{tBu}Fe(SPh)(N)]^{n-}$ (n = 3, 2, 1) suggests that the XAS pre-edge feature is a useful tool for identifying the metal oxidation state as changes in both pre-edge energy (0.5 eV) and intensity are observed. The V2C XES region does not change noticeably, in energy or intensity, upon changing oxidation state on the metal. These results thus argue that XAS pre-edges provide a more useful probe of oxidation state.

(3) The V2C XES spectra are extremely sensitive to ligand identity, particularly the Kβ″ emission line (X 2s → Fe 1s). This XES Kβ″ feature can distinguish similar scatterers, such as C, N, and O coordinated to the metal center, with observed shifts of ∼7 eV in the energy of the Kβ″ feature across this series. The differentiation of light atoms is often quite difficult using other techniques, such as XAS, EXAFS, or crystallography and, thus, highlights a strength of V2C XES.

(4) The V2C XES Kβ″ intensity is exponentially related to the Fe−X bond lengths and linearly related to the percent of Fe np character. Thus, by combining this information with point 3 above, one can spectroscopically define possible structures and test these against DFT calculations. In this way, V2C XES data provide a means to limit the number of possible models in an EXAFS data analysis. However, it is important to note that, at longer metal−ligand bond distances, the Kβ″ features may become too weak to be observed (Figure 7A). The threshold for observation of Kβ″ intensity will depend on both the nature of the ligand and the bonding interaction.

In summary, by combining XAS and XES techniques with DFT, a more complete picture of transition-metal geometric and electronic structure can be achieved. With the advent of more intense synchrotron sources and better-optimized spectrometers for emission measurements, one can envision that combined XAS and XES approaches will become more routine and have the potential to significantly contribute to our understanding of transition-metal-mediated catalysis.

ASSOCIATED CONTENT

Supporting Information

Example ORCA input files for geometry optimizations, and XAS and XES calculations. This material is available free of charge via the Internet at http://pubs.acs.org.

AUTHOR INFORMATION

Corresponding Author

*E-mail: holland@chem.rochester.edu (P.L.H.); serena.debeer@cec.mpg.de (S.D.).

Notes

The authors declare no competing financial interest.

■ ACKNOWLEDGMENTS

S.D. thanks the Max Planck Society and Cornell University for funding and the Sloan Foundation for a fellowship. P.L.H. and U.B. thank the National Institutes of Health for funding (GM-065313, P.L.H. and P41GM103393, U.B.). Portions of the research were carried out at the Stanford Synchrotron Radiation Lightsource, a national user facility operated by Stanford University on behalf of the DOE, BES. The SSRL SMB Program is supported by DOE, BER and NIH, NCRR, BMTP.

■ REFERENCES

(1) Heaton, B. *Mechanisms in Homogeneous Catalysis*; Wiley-VCH Verlag GmbH & Co. KGaA: Weinheim, 2005.
(2) McAlpin, J. G.; Surendranath, Y.; Dinca, M.; Stich, T. A.; Stoian, S. A.; Casey, W. H.; Nocera, D. G.; Britt, R. D. *J. Am. Chem. Soc.* **2010**, *132*, 6882.
(3) Solomon, E. I.; Szilagyi, R. K.; DeBeer George, S.; Basumallick, L. *Chem. Rev.* **2004**, *104*, 419.
(4) Hoffman, B. M.; Dean, D. R.; Seefeldt, L. C. *Acc. Chem. Res.* **2009**, *42*, 609.
(5) de Groot, F. *Chem. Rev.* **2001**, *101*, 1779.
(6) Kanan, M. W.; Yano, J.; Surendranath, Y.; Dinca, M.; Yachandra, V. K.; Nocera, D. G. *J. Am. Chem. Soc.* **2010**, *132*, 13692.
(7) DuBois, J. L.; Mukherjee, P.; Collier, A. M.; Mayer, J. M.; Solomon, E. I.; Hedman, B.; Stack, T. D. P.; Hodgson, K. O. *J. Am. Chem. Soc.* **1997**, *119*, 8578.
(8) Eitel, S. H.; Bauer, M.; Schweinfurth, D.; Deibel, N.; Sarkar, B.; Kelm, H.; Krüger, H.-J.; Frey, W.; Peters, R. *J. Am. Chem. Soc.* **2012**, *134*, 4683.
(9) Fox, S.; Nanthakumar, A.; Wikström, M.; Karlin, K. D.; Blackburn, N. J. *J. Am. Chem. Soc.* **1996**, *118*, 24.
(10) Lo, F.-C.; Lee, J.-F.; Liaw, W.-F.; Hsu, I.-J.; Tsai, Y.-F.; Chan, S. I.; Yu, S. S.-F. *Chem.—Eur. J.* **2012**, *18*, 2565.
(11) Pandya, K. I.; Koningsberger, D. C. *Physica B* **1989**, *158*, 386.
(12) Delgado-Jaime, M. U.; Dible, B. R.; Chiang, K. P.; Brennessel, W. W.; Bergmann, U.; Holland, P. L.; DeBeer, S. *Inorg. Chem.* **2011**, *50*, 10709.
(13) Chandrasekaran, P.; Stieber, S. C. E.; Collins, T. J.; Que, L., Jr.; Neese, F.; DeBeer, S. *Dalton Trans.* **2011**, *40*, 11070.
(14) Stone, K. L.; Behan, R. K.; Green, M. T. *Proc. Natl. Acad. Sci. U.S.A.* **2005**, *102*, 16563.
(15) Lee, N.; Petrenko, T.; Bergmann, U.; Neese, F.; DeBeer, S. *J. Am. Chem. Soc.* **2010**, *132*, 9715.
(16) Doonan, C. J.; Zhang, L.; Young, C. G.; George, S. J.; Deb, A.; Bergmann, U.; George, G. N.; Cramer, S. P. *Inorg. Chem.* **2005**, *44*, 2579.
(17) Seljakow, N.; Krasnikow, A. *Z. Phys. A* **1925**, *33*, 601.
(18) Tsutsumi, K. *J. Phys. Soc. Jpn.* **1959**, *14*, 1696.
(19) Glatzel, P.; Bergmann, U. *Coord. Chem. Rev.* **2005**, *249*, 65.
(20) Pollock, C. J.; DeBeer, S. *J. Am. Chem. Soc.* **2011**, *133*, 5594.
(21) Lancaster, K. M.; Finkelstein, K. D.; DeBeer, S. *Inorg. Chem.* **2011**, *50*, 6767.
(22) Pushkar, Y.; Long, X.; Glatzel, P.; Brudvig, G. W.; Dismukes, G. C.; Collins, T. J.; Yachandra, V. K.; Yano, J.; Bergmann, U. *Angew. Chem., Int. Ed.* **2010**, *49*, 800.
(23) Smolentsev, G.; Soldatov, A. V.; Messinger, J.; Merz, K.; Weyhermüller, T.; Bergmann, U.; Pushkar, Y.; Yano, J.; Yachandra, V. K.; Glatzel, P. *J. Am. Chem. Soc.* **2009**, *131*, 13161.
(24) Swarbrick, J. C.; Kvashnin, Y.; Schulte, K.; Seenivasan, K.; Lamberti, C.; Glatzel, P. *Inorg. Chem.* **2010**, *49*, 8323.
(25) Lancaster, K. M.; Roemelt, M.; Ettenhuber, P.; Hu, Y.; Ribbe, M. W.; Neese, F.; Bergmann, U.; DeBeer, S. *Science* **2011**, *334*, 974.
(26) Chiang, K. P.; Barrett, P. M.; Ding, F.; Smith, J. M.; Kingsley, S.; Brennessel, W. W.; Clark, M. M.; Lachicotte, R. J.; Holland, P. L. *Inorg. Chem.* **2009**, *48*, 5106.
(27) Strautmann, J. B. H.; DeBeer George, S.; Bothe, E.; Bill, E.; Weyhermüller, T.; Stammler, A.; Bögge, H.; Glaser, T. *Inorg. Chem.* **2008**, *47*, 6804.
(28) George, G. N. *EXAFSPAK*; Stanford Synchrotron Radiation Laboratory, Standord Linear Accelerator Center, Stanford Univerity: Stanford, CA, 2001.
(29) Neese, F. *WIREs: Comput. Mol. Sci.* **2012**, *2*, 73.
(30) Becke, A. D. *Phys. Rev. A* **1988**, *38*, 3098.
(31) Perdew, J. P. *Phys. Rev. B* **1986**, *33*, 8822.
(32) Pantazis, D. A.; Chen, X. Y.; Landis, C. R.; Neese, F. *J. Chem. Theory Comput.* **2008**, *4*, 908.
(33) van Lenthe, E.; van der Avoird, A.; Wormer, P. E. S. *J. Chem. Phys.* **1998**, *108*, 4783.
(34) Klamt, A.; Schüürmann, G. *J. Chem. Soc., Perkin Trans. 2* **1993**, 799.
(35) Pettersen, E. F.; Goddard, T. D.; Huang, C. C.; Couch, G. S.; Greenblatt, D. M.; Meng, E. C.; Ferrin, T. C. *J. Comput. Chem.* **2004**, *13*, 1605.
(36) Delgado-Jaime, M. U.; DeBeer, S. *J. Comput. Chem.* **2012**, DOI: 10.1002/jcc.23028.
(37) Yang, L.; Powell, D. R.; Houser, R. P. *Dalton Trans.* **2007**, 955.
(38) Neese, F. *Inorg. Chim. Acta* **2002**, *337*, 181.
(39) Westre, T. E.; Kennepohl, P.; DeWitt, J. G.; Hedman, B.; Hodgson, K. O.; Solomon, E. I. *J. Am. Chem. Soc.* **1997**, *119*, 6297.
(40) Kau, L. S.; Spira-solomon, D. J.; Pennerhahn, J. E.; Hodgson, K. O.; Solomon, E. I. *J. Am. Chem. Soc.* **1987**, *109*, 6433.
(41) Shadle, S. E.; Penner-Hahn, J. E.; Schugar, H. J.; Hedman, B.; Hodgson, K. O.; Solomon, E. I. *J. Am. Chem. Soc.* **1993**, *115*, 767.
(42) Roemelt, M.; Beckwith, M. A.; Duboc, C.; Collomb, M.-N.; Neese, F.; DeBeer, S. *Inorg. Chem.* **2012**, *51*, 680.
(43) Stieber, S. C. E.; Milsmann, C.; Hoyt, J. M.; Turner, Z. R.; Finkelstein, K. D.; Wieghardt, K.; DeBeer, S.; Chirik, P. J. *Inorg. Chem.* **2012**, *51*, 3770.
(44) DeBeer George, S.; Petrenko, T.; Neese, F. *J. Phy. Chem. A* **2008**, *112*, 12936.
(45) Mijovilovich, A.; Hayashi, H.; Kawamura, N.; Osawa, H.; Bruijnincx, P. C. A.; Klein Gebbink, R. J. M.; de Groot, F. M. F.; Weckhuysen, B. M. *Eur. J. Inorg. Chem.* **2012**, 1589.
(46) Atkins, A. J.; Jacob, C. R.; Bauer, M. *Chem.—Eur. J.* **2012**, *18*, 7021.
(47) Vanko, G.; Neisius, T.; Molnar, G.; Renz, F.; Karpati, S.; Shukla, A.; de Groot, F. M. F. *J. Phy. Chem. B* **2006**, *110*, 11647.
(48) Beckwith, M. A.; Roemelt, M.; Collomb, M.-N.; DuBoc, C.; Weng, T.-C.; Bergmann, U.; Glatzel, P.; Neese, F.; DeBeer, S. *Inorg. Chem.* **2011**, *50*, 8397.
(49) Bergmann, U.; Horne, C. R.; Collins, T. J.; Workman, J. M.; Cramer, S. P. *Chem. Phys. Lett.* **1999**, *302*, 119.
(50) Rodriguez, M. M.; Bill, E.; Brennessel, W. W.; Holland, P. L. *Science* **2011**, *334*, 780.
(51) Hoffman, B. M.; Lukoyanov, D.; Dean, D. R.; Seefeldt, L. C. *Acc. Chem. Res.* **2013**, *46*, 587.
(52) Tolman, W. B. *Activation of Small Molecules: Organmetallic and Bioinorganic Perspectives*; Wiley-VCH: Germany 2006.
(53) Nam, W. *Acc. Chem. Res.* **2007**, *40*, 522.
(54) Kovaleva, E. G.; Neibergall, M. B.; Chakrabarty, S.; Lipscomb, J. D. *Acc. Chem. Res.* **2007**, *40*, 475.
(55) Hopfl, H. *J. Organomet. Chem.* **1999**, *581*, 129.
(56) Vela, J.; Cirera, J.; Smith, J. M.; Lachicotte, R. J.; Flaschenriem, C. J.; Alvarez, S.; Holland, P. L. *Inorg. Chem.* **2007**, *46*, 60.
(57) Hutchison, A. R.; Mitra, A.; Atwood, D. A. *Main Group Chem.* **2005**, *4*, 187.
(58) DeBeer George, S.; Brant, P.; Solomon, E. I. *J. Am. Chem. Soc.* **2005**, *127*, 667.
(59) Berry, J. F.; Bill, E.; Bothe, E.; DeBeer George, S.; Mienert, B.; Neese, F.; Wieghardt, K. *Science* **2006**, *312*, 1937.
(60) Kropp, H.; King, A. E.; Khusniyarov, M. M.; Heinemann, F. W.; Lancaster, K. M.; DeBeer, S.; Bill, E.; Meyer, K. *J. Am. Chem. Soc.* **2012**, *134*, 15538.

(61) Berry, J. F.; DeBeer George, S.; Neese, F. *Phys. Chem. Chem. Phys.* **2008**, *10*, 4361.
(62) Millikan, R. A.; Bowun, I. S. *Proc. Natl. Acad. Sci. U.S.A.* **1927**, *13*, 531.